

## Laser studies of near-resonant state-changing collisions of calcium ( $4s6s\ ^1S_0$ ) with the rare gases

Michael O. Hale and Stephen R. Leone\*

*Joint Institute for Laboratory Astrophysics, National Bureau of Standards and University of Colorado, Boulder, Colorado 80309*

*and Department of Chemistry, University of Colorado, Boulder, Colorado 80309*

(Received 19 July 1984)

State-changing collisions of  $\text{Ca}(4s6s\ ^1S_0)$  with the rare gases are studied by pulsed laser excitation and time- and wavelength-resolved detection. The total depletion rates of the  $4s6s\ ^1S_0$  state with different rare gases vary by over a factor 10, with the lighter rare gases being markedly more efficient than the heavier ones. Relative branching ratios to the specific near-resonant, energy-transfer product states,  $4p4p\ ^1D_2$  ( $\Delta E = -29\ \text{cm}^{-1}$ ),  $3d4p\ ^1F_3$  ( $\Delta E = 152\ \text{cm}^{-1}$ ), and  $4s6s\ ^3S_1$  ( $\Delta E = 216\ \text{cm}^{-1}$ ), are measured for  $^3\text{He}$ ,  $^4\text{He}$ , Ne, and Xe. Transfer to the  $^1D_2$  state is always the major relaxation pathway. The rate constant for  $^3S_1$  production is immeasurably small, implying a small spin-orbit matrix element for curve crossing that leads to a spin change. The results for  $4p4p\ ^1D_2$  production are compared with simple theoretical calculations based on established models for near-resonant energy transfer between states which are coupled at large internuclear distance. These models successfully explain the dominant transfer to the  $4p4p\ ^1D_2$  state and the trends with rare gas, which are attributed largely to enhancement of the near-resonant-transfer process with increasing velocity. The effects of wave-function mixing in the isolated atom (e.g., spin mixing) on the general outcome of state-changing collisions in two-electron atoms are discussed. Two-electron atoms offer numerous possibilities for further testing of theories of near-resonant energy transfer.

### I. INTRODUCTION

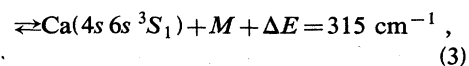
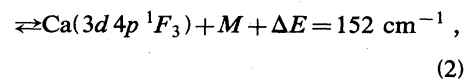
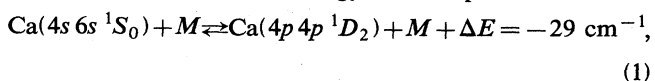
Collisional energy transfer in atomic metal vapors is a subject of much attention in the literature.<sup>1-7</sup> Extensive studies on the one-electron alkali-metal-rare-gas systems have provided a large amount of rate information, which has been systematized and used to determine the basic mechanisms involved.<sup>1-3</sup> Two-electron alkaline-earth-rare-gas collision systems have only recently received more attention,<sup>4-7</sup> and the mechanisms involved are not as well understood. In two-electron atoms there are collision processes which have no analog in the alkali-metal-rare-gas systems (e.g., spin changing), and there is often a high degree of spin mixing and configuration interaction between states in the isolated atoms.<sup>8</sup> For this reason it is of interest to study collisional transfer between states with relatively well-known amounts of spin mixing and configuration interaction in order to determine what, if any, effect these interactions have on the energy-transfer process.

Spin-changing collisions have recently been studied in atomic calcium and cadmium collisions with a variety of collision partners including the spherically symmetric rare gases.<sup>4-7</sup> In all of these studies energy transfer is observed from an excited  $^1P_1$  state to a nearby  $^3P_j$  multiplet. Relatively large cross sections are observed and the distribution of product  $j$  states is sometimes nonstatistical. However, in all of these studies there is already a significant amount of spin mixing in the isolated atomic states, and it is unknown whether a true spin-changing ( $^1P$  part of the initial state to  $^3P$  product state) or fine-structure-like-changing ( $^3P$  part of the initial state to  $^3P$  product

state) mechanism is occurring for  $^1S_0$  perturbers. As discussed below, there are other states in these atoms with a small initial amount of spin mixing, which can better serve to test the magnitude of the true spin-changing interaction.

The effect of configuration interaction on collisional energy transfer has received little or no attention in the literature. This is surprising considering how important this effect is in isolated atoms and their spectroscopy.<sup>8</sup> As in optical spectroscopy, collisional matrix elements typically do not couple states differing by a change of more than one quantum number in the electron configuration with first-order perturbation theory and a change of two with second-order perturbation theory. Thus the effects of configuration interaction could play a significant role in the energy-transfer processes that are "allowed."

In this paper we report an experimental study of near-resonant energy transfer among calcium excited states upon collision with rare gases. In several cases the amount of spin mixing and configuration interaction is approximately known for the initial and final states. The initially excited state is the  $4s6s\ ^1S_0$  state of calcium and the various near-resonant energy-transfer processes are



where  $M = {}^3\text{He}$ ,  ${}^4\text{He}$ , Ne, Ar, Kr, and Xe and  $\Delta E$  is the energy between the initial and final states. The time- and wavelength-resolved detection techniques developed in our earlier work<sup>7</sup> allow an accurate determination of the total  ${}^1S_0$  energy-transfer rate constants, the radiative lifetimes, the branching ratios to individual product states, and thus the individual forward rate constants. The time-resolved technique directly obtains the necessary radiative rates, giving a significant advantage over steady-state fluorescence intensity methods, where prior knowledge of these quantities may be required.

The relative amounts of spin mixing and configuration interaction for the  $4s6s {}^1S_0$  and  $4s6s {}^3S_1$  levels are known from measurements of the  $4sns {}^1S_0$  and  $4sns {}^3S_1$  Rydberg series of calcium.<sup>9-11</sup> Although there is significant configuration interaction between the  $4s6s {}^1S_0$  and  $4p4p {}^1S_0$  states, it is unlikely that this will have a great effect on the rates of the dominant  ${}^1S_0 \rightarrow {}^1D_2$  process, since both configurations of  ${}^1S_0$  can couple to the  ${}^1D_2$  configuration by second-order induced-dipole potentials. None of the singlet states,  ${}^1S$ ,  ${}^1F$ , or  ${}^1D$ , is observed to be perturbed by nearby triplet states, nor do they perturb the triplet Rydberg series. Thus these states are assumed to be relatively pure singlet states. The  $4s6s {}^3S_1$  state fits into its Rydberg series very well, implying that this level does not mix significantly with any of the nearby singlet states. Thus any observed  $4s6s {}^1S_0 - 4s6s {}^3S_1$  energy transfer must be due primarily to spin-orbit interactions.

The mechanisms of energy transfer in atomic state-changing collisions are typically considered as local curve crossing events; however, in cases of very near resonance, energy transfer can occur over a long range of distances due to perturbations from the weak van der Waals-type interactions. This is especially the case for the near-resonant process (1), in which the wave functions of the isolated atomic states are mixed with other calcium states and the initial  ${}^1S_0$  and final  ${}^1D_2$  states are pushed close together in energy. The configurations of these mixed states can be coupled with second-order induced-dipole interactions. Simple theoretical calculations using a two-state approximation and  $-A/R^n$  forces are compared to the measured rate constants. These calculations are based on the formalisms of Bates,<sup>12</sup> Vainshtein *et al.*,<sup>13</sup> and Presnyakov<sup>14</sup> for near-resonant energy transfer with standard long-range matrix elements.<sup>15</sup> The agreement with experimental results is good and shows the distinctive trend in rate constants observed for the rare-gas series (i.e., decreasing markedly with increased reduced mass). The values of the forward rate constants into each state are further discussed in terms of the amounts of spin mixing and configuration interaction involved in these states.

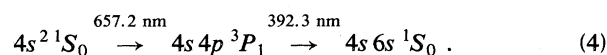
## II. EXPERIMENTAL SETUP

The experimental apparatus has been described in detail in a previous publication,<sup>7</sup> the only modification being the incorporation of a second laser for two-step excitation. The method uses pulsed laser excitation of various excited states of calcium atoms contained in a high-temperature cell. Time-resolved fluorescence is detected from either the initially populated or collisionally populated states by

a fast photomultiplier tube (PMT), which views the cell through a monochromator or a narrow bandpass filter. The output of the PMT is recorded by a transient digitizer or a boxcar integrator, and the data are transferred to a minicomputer for analysis.

There are three lasers used in this experiment. The first is a flashlamp-pumped dye laser operating on Rhodamine-6G. This laser is operated with an etalon producing 5 mJ, 2  $\mu\text{s}$  pulses with a full width at half maximum (FWHM) of 1  $\text{cm}^{-1}$  and a repetition rate of 10 Hz. The second and third lasers are both Nd:yttrium-aluminum-garnet (YAG)-pumped dye lasers. One, a commercial dye laser, produces 6 ns, 0.3  $\text{cm}^{-1}$  FWHM pulses with a typical output power at 392.3 and 422.6 nm of 0.2–5 mJ when pumped by the third harmonic of the YAG (355 nm). The other dye laser is homebuilt and produces 6 ns, 10  $\text{cm}^{-1}$  FWHM pulses with a typical power of 2 mJ at 586.7 nm.

Figure 1 is a partial energy-level diagram of atomic calcium showing the excitation schemes and important radiative pathways from the excited states involved.<sup>11</sup> Only the  ${}^1D_2$ ,  ${}^1F_3$ , and  ${}^3S_1$  are expected to be collisionally populated since all other levels are more than 1000  $\text{cm}^{-1}$  away. The  $3d4p {}^3P_j$  (1355  $\text{cm}^{-1}$  below),  $4p^2 {}^3P_j$  (2226  $\text{cm}^{-1}$  below), and  $3d4p {}^3D_j$  (2471  $\text{cm}^{-1}$  below) are searched for but not observed in emission until the rare-gas pressure is very large ( $\sim 3.0 \times 10^{17} \text{ cm}^{-3}$ ). Since the  ${}^1S_0$  state has only one strong visible transition to the  $4s4p {}^1P_1$  state at 586.7 nm, which is used to monitor emission, the  ${}^1S_0$  state is typically excited by the two-step process through the  $4s4p {}^3P_1$  state:



This allows us to observe  ${}^1S_0$  emission on the 586.7-nm line or emission from the nearby  ${}^1D_2$  at 585.7 nm without

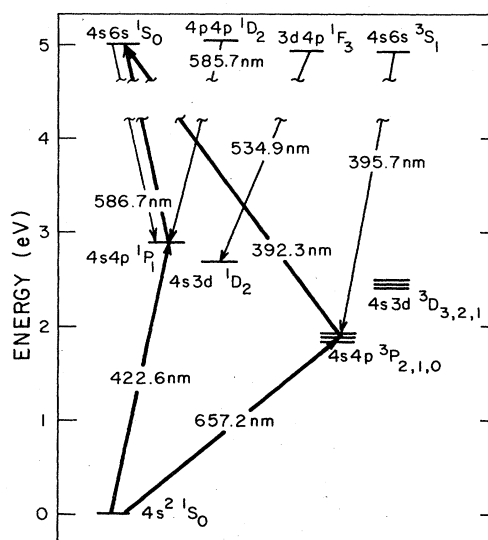
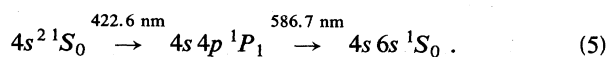


FIG. 1. Partial energy-level diagram of atomic calcium. Only relevant energy levels and transitions are shown. Arrows indicate transitions used for laser pumping (thick lines) or fluorescence monitoring (thin lines).

intense scattered laser light. Since the first state,  $^3P_1$ , is a long-lived metastable, the first laser is the 1  $\mu$ s dye laser and the second laser is the commercial YAG-pumped dye laser. The second laser is delayed from the first by approximately 2  $\mu$ s to reduce scattered light. The total quenching rates for  $^1S_0$  as a function of buffer-gas pressure are determined from the  $^1S_0$  lifetime as measured from the  $4s6s\ ^1S_0 \rightarrow 4s4p\ ^1P_1$  transition at 586.7 nm through a monochromator. The same pumping scheme is also used when measuring the relative branching ratio for  $^1S_0$  transfer to  $^1D_2$  and  $^1F_3$ . To obtain this branching ratio, fluorescence intensity is measured on the  $4p4p\ ^1D_2 \rightarrow 4s4p\ ^1P_1$  and  $3d4p\ ^1F_3 \rightarrow 4s3d\ ^1D_2$  transitions at 585.7 and 534.7 nm, respectively, again through a monochromator. The second pumping scheme uses the two YAG-pumped dye lasers:



This pumping scheme can populate a greater fraction into the  $4s6s\ ^1S_0$  level and is used in measuring the relative branching ratio from  $^1S_0$  to  $^3S_1$  and  $^1F_3$  by monitoring the  $4s6s\ ^3S_1 \rightarrow 4s4p\ ^3P_1$  and  $3d4p\ ^1F_3 \rightarrow 4s3d\ ^1D_2$  transitions at 395.7 and 534.7 nm, respectively, where scattered light from the lasers does not interfere.

The  $^1S_0$  radiative lifetime is measured at near zero buffer-gas pressures ( $< 10$  Pa) by signal averaging with a transient digitizer the fluorescence from the  $^1S_0$  state that is selected by a narrow bandpass interference filter. Measurements of the  $^1S_0$  lifetime and total quenching data that are taken at buffer-gas pressures greater than 10 Pa, where collisional emission from other states becomes important, are directly signal averaged with the transient digitizer by observing the  $^1S_0$  emission through the monochromator. An instrumental baseline is subtracted from these data resulting in a signal-to-noise of approximately 5 after 320–640 pulses. The individual transitions for the branching-ratio measurements are measured by scanning over the emission lines with the monochromator. The fluorescence intensity of collisional product states is determined by integrating a 15 ns portion of the fluorescence at  $t = 50$  ns with a boxcar averager as the monochromator is scanned. The gate width and the starting time are chosen to maximize product signal intensity at low buffer-gas densities. This integrated portion is normalized to both laser power and laser excitation efficiencies by monitoring the total fluorescence intensity of two given lines through a narrow bandpass filter. The  $4s6s\ ^1S_0 \rightarrow 4s4p\ ^1P_1$  transition at 586.7 nm is monitored to normalize for laser excitation efficiencies at buffer-gas pressures below  $10^2$  Pa, where most of the excited-state population resides in the  $^1S_0$  state, and the  $3d4p\ ^1F_3 \rightarrow 4s3d\ ^1D_2$  transition is used for the normalization at buffer-gas pressures above  $10^2$  Pa, where most of the excited-state population resides in the product states.

The calcium oven<sup>7</sup> consists of a separately heated interaction region and a calcium reservoir. The interaction region is maintained between 773 and 823 K and the calcium reservoir is maintained between 748 and 798 K, giving a calcium density of less than  $3 \times 10^{12}$  atoms/cm<sup>3</sup>. Research-grade calcium and rare gases are used with no

further purification. The pressures of the rare gases are measured by a 0– $10^3$ -Pa capacitance manometer and the calcium densities are determined from vapor-pressure curves.<sup>16</sup>

### III. KINETICS

The basic kinetics of the time-dependent measurement of total energy-transfer rates and branching ratios using a pulsed laser are described in an earlier article.<sup>7</sup> Following pulsed laser excitation of the  $4s6s\ ^1S_0$  state, there are several different radiative and collisional pathways of importance. We assume and confirm experimentally that transfer to the states nearest in energy predominate over all other relaxation pathways. Figure 1 shows the main radiative pathways from the levels involved. The  $4s6s\ ^1S_0$  and  $4p4p\ ^1D_2$  levels radiate primarily to the  $4s5p\ ^1P_1$  and  $4s4p\ ^1P_1$  states. The radiative branching ratios to these levels are similar for both initial levels.<sup>17</sup> The  $4s6s\ ^3S_1$  state radiates to the  $4s5p\ ^3P_j$  and  $4s4p\ ^3P_j$  levels with a radiative branching ratio of about 1:3, respectively.<sup>17</sup> This ratio is important for the measurement of the collisional transfer from  $^1S_0$  to  $^3S_1$ , which is found to be negligibly small. The  $3d4p\ ^1F_3$  state emits exclusively to the  $4s3d\ ^1D_2$  state. The total radiative rates for the  $^1S_0$ ,  $^1D_2$ ,  $^1F_3$ , and  $^3S_1$  states will be denoted  $\Gamma_{(^1S)}$ ,  $\Gamma_{(^1D)}$ ,  $\Gamma_{(^1F)}$ , and  $\Gamma_{(^3S)}$ , respectively.

The collisional pathways are identified in processes (1)–(3) above. The  $^1D_2$  level is 29  $\text{cm}^{-1}$  above the  $^1S_0$  while the  $^1F_3$  and  $^3S_1$  levels are 152 and 215  $\text{cm}^{-1}$  below the  $^1S_0$  level, respectively. The individual forward rate constants from  $^1S_0$  to  $^1D_2$ ,  $^1F_3$ , and  $^3S_1$  will be denoted as  $k_{(^1S \rightarrow ^1D)}$ ,  $k_{(^1S \rightarrow ^1F)}$ , and  $k_{(^1S \rightarrow ^3S)}$ . A total quenching rate constant for  $^1S_0$  is defined as  $k_q$  which is the sum of all forward and backward rates from the  $^1S_0$  level to all other product states. A measurement of  $k_q$  and the relative magnitudes of the individual forward rate constants together with detailed balancing provides sufficient information to determine the absolute magnitude of the individual forward rates.

Only the low and high buffer-gas density limits to the kinetics are needed to determine the rate constants and radiative lifetimes. In the low-pressure limit where the buffer-gas density  $[M]$  times the total quenching rate is much smaller than the radiative lifetime of  $^1S_0$ , the time dependence of the initial state is

$$[^1S_0] \cong [^1S_0]_0 \exp\{-(\Gamma_{(^1S)} + k_q[M])t\}, \quad (6)$$

where  $[^1S_0]_0$  is the initial population of the  $^1S_0$  state. The time dependence of any one of the product states is

$$[^1D_2] \cong \frac{[^1S_0]_0 k_{(^1S \rightarrow ^1D)} [M]}{\Gamma_{(^1S)} - \Gamma_{(^1D)}} \times \{\exp(-\Gamma_{(^1D)}t) - \exp[-(\Gamma_{(^1S)}t)]\}. \quad (7)$$

Here we have chosen the  $^1D_2$  state as an example product state. Equation (7) also applies to the  $^1F_3$  and  $^3S_1$  states with appropriate changes of rate constants. The total

quenching rate of the  $^1S_0$  state is easily measured from its single exponential decay ( $\tau_{\text{obs}}$ ) as a function of buffer-gas density. A plot of  $1/\tau_{\text{obs}}$  versus  $[M]$  has slope  $k_q$  and intercept  $\Gamma_{(^1S)}$ . As a check of this technique,  $\Gamma_{(^1S)}$  is also measured at  $[M]=0$ .

Relative branching ratios are somewhat more difficult to measure than the total quenching rates. A time window (50–65 ns relative to the laser excitation at  $t=0$  ns) of the product state emission is integrated and then divided by the total emission intensity from either  $^1S_0$  or  $^1F_3$  in order to normalize for laser excitation efficiencies, giving an intensity  $I$ . The normalization is done using the  $^1S_0$  emission at low buffer-gas pressures and the  $^1F_3$  emission at high buffer-gas pressure, since most of the population resides in either of these two states in the two limits, respectively. As was shown in our earlier work<sup>7</sup> the windowed portion of Eq. (7) is just equal to Eq. (7) times  $c_i \Delta t$ , where  $c_i$  is an experimental detection factor and  $\Delta t$  is the duration of the integration. If, in the low-pressure (LP) limit, one divides the integrated intensity of two lines, say  $^1D_2$  and  $^1F_3$ , then one gets at low buffer-gas pressures

$$\left( \frac{I_{(^1D)}}{I_{(^1F)}} \right)_{\text{LP}} = \frac{c_{(^1D)} k_{(^1S \rightarrow ^1D)}}{c_{(^1F)} k_{(^1S \rightarrow ^1F)}} \left[ \frac{\Gamma_{(^1S)} - \Gamma_{(^1F)}}{\Gamma_{(^1S)} - \Gamma_{(^1D)}} \right] \times \left[ \frac{\exp(-\Gamma_{(^1D)} t_1) - \exp(-\Gamma_{(^1S)} - t_1)}{\exp(-\Gamma_{(^1F)} t_1) - \exp(-\Gamma_{(^1S)} t_1)} \right]. \quad (8)$$

In the high-pressure (HP) limit the  $^1D_2$  and  $^1F_3$  states are completely in equilibrium at time  $t_1$ , the onset of the integration window, and one gets

$$\left( \frac{I_{(^1D)}}{I_{(^1F)}} \right)_{\text{HP}} = \frac{c_{(^1D)} g_{(^1D)}}{c_{(^1F)} g_{(^1F)}} e^{-\Delta E/k_B T}. \quad (9)$$

Here  $g_{(^1D)}$  and  $g_{(^1F)}$  are the degeneracies of the  $^1D_2$  and  $^1F_3$  states, respectively, and  $\Delta E$  is the energy difference between these two states. A measure of  $(I_{(^1D)}/I_{(^1F)})_{\text{HP}}$  thus reveals  $c_{(^1D)}/c_{(^1F)}$ , which can be used along with the data for  $(I_{(^1D)}/I_{(^1F)})_{\text{LP}}$  and with the directly measured state lifetimes to determine the ratio of rates  $k_{(^1S \rightarrow ^1D)}/k_{(^1S \rightarrow ^1F)}$ . The branching ratios are extracted from the zero-pressure intercepts. In Eq. (8) it is found that a 30% error in any given lifetime gives rise to only a 16% error in the final ratio of rates. This significantly reduces the error bars in the ratio of rates, which are due primarily to the errors in the zero-pressure intercept of the intensity ratios.

Since the detection factors  $c_i$  are independent of rare gas, they need to be measured for only one rare gas. In this calibration the ratio  $I_{(^1D)}/I_{(^1F)}$  is measured for neon as a function of pressure and the ratio of  $c_i$ 's is extracted in the high-pressure limit. The ratio  $k_{(^1S \rightarrow ^1D)}/k_{(^1S \rightarrow ^1F)}$  is

determined in the low-pressure limit where single collision events predominate. Empirically the proper low-pressure limit depends on the time and duration of the detection time window used, and for our conditions a pressure of 10 Pa is found to be low enough. The intensity ratio is measured for the other rare gases (RG) at pressures of about 10 Pa (low-pressure limit) and the relationship

$$\frac{(I_{(^1D)}/I_{(^1F)})_{\text{RG}}}{(I_{(^1D)}/I_{(^1F)})_{\text{Ne}}} \cong \frac{(k_{(^1S \rightarrow ^1D)}/k_{(^1S \rightarrow ^1F)})_{\text{RG}}}{(k_{(^1S \rightarrow ^1D)}/k_{(^1S \rightarrow ^1F)})_{\text{Ne}}} \quad (10)$$

is used to determine the ratio of rates for the other rare gases.

The ratio  $k_{(^1S \rightarrow ^3S)}/k_{(^1S \rightarrow ^1F)}$  gives a measure of the spin-changing efficiency. However, emission from the  $^3S_1$  state upon transfer from  $^1S_0$  is not observed at any buffer-gas pressures. Thus, we make an estimate of the maximum possible  $^3S_1$  intensity from the noise in the spectrum. If the forward rates were determined just by statistical weighting factors ( $k_{(^1S \rightarrow ^3S)}/k_{(^1S \rightarrow ^1F)}$ ) =  $g_{(^3S)}/g_{(^1F)}$  then at the buffer-gas pressures used in these experiments, the  $^3S$  and  $^1F$  states would be in equilibrium and the expected  $^3S_1$  intensity can be estimated relative to the  $^1F_3$  intensity from

$$I_{(^3S)} = \frac{g_{(^3S)} \eta_{\text{PMT}}(^3S) \tau_{(^1F)} b_r(^3S)}{g_{(^1F)} \eta_{\text{PMT}}(^1F) \tau_{(^3S)} b_r(^1F)} I_{(^1F)}, \quad (11)$$

where  $\eta_{\text{PMT}}(x)$  is the PMT quantum efficiency,  $\tau_{(x)}$  is the lifetime of the state, and  $b_r(x)$  is the radiative branching ratio for the transition observed. For our system with  $\eta_{\text{PMT}}(^3S)/\eta_{\text{PMT}}(^1F) = \frac{12}{5}$  (quantum efficiencies taken from manufacturer's data),  $\tau_{(^1F)}/\tau_{(^1S)} \cong 1$ , and  $b_r(^3S)/b_r(^1F) \cong 0.25$ , one would find  $I_{(^3S)}/I_{(^1F)} = 0.26$ , assuming there are no other pathways for loss of  $^3S$  or  $^1F$ . Experimentally  $I_{(^3S)}$  is smaller than the baseline noise in the spectra taken at  $1.5 \times 10^3$  Pa pressure of Ne. Thus  $I_{(^3S)}/I_{(^1F)}$  (measured)  $< 0.001$ , which means that the ratio of rates to  $^3S/1F$  is at least 0.001/0.26 times smaller than a statistical branching.

From the total energy-transfer rates and ratios of forward rates the magnitude of the individual forward rates are determined. Using detailed balancing, we can write the total rate constant as

$$k_q = k_{(^1S \rightarrow ^1D)} \left[ 1 + \frac{g_{(^1S)}}{g_{(^1D)}} e^{-\Delta E/k_B T} \right] + k_{(^1S \rightarrow ^1F)} \left[ 1 + \frac{g_{(^1S)}}{g_{(^1F)}} e^{-\Delta E/k_B T} \right] + k_{(^1S \rightarrow ^3S)} \left[ 1 + \frac{g_{(^1S)}}{g_{(^3S)}} e^{-\Delta E/k_B T} \right]. \quad (12)$$

Inserting the measured quantities  $k_{(^1S \rightarrow i)}/k_{(^1S \rightarrow j)}$  one gets

$$\begin{aligned}
 k_q = k_{(1S \rightarrow 1D)} & \left[ \left[ 1 + \frac{g_{(1S)}}{g_{(1D)}} e^{-\Delta E/k_B T} \right] \right. \\
 & + \frac{k_{(1S \rightarrow 1F)}}{k_{(1S \rightarrow 1D)}} \left[ 1 + \frac{g_{(1S)}}{g_{(1D)}} e^{-\Delta E/k_B T} \right] \\
 & + \left[ \frac{k_{(1S \rightarrow 1F)}}{k_{(1S \rightarrow 1D)}} \right] \left[ \frac{k_{(1S \rightarrow 3S)}}{k_{(1S \rightarrow 1F)}} \right] \\
 & \left. \times \left[ 1 + \frac{g_{(1S)}}{g_{(3S)}} e^{-\Delta E/k_B T} \right] \right] . \quad (13)
 \end{aligned}$$

This equation is then solved for  $k_{(1S \rightarrow 1D)}$  in terms of the measured quantities  $k_q$ ,  $k_{(1S \rightarrow 1F)}/k_{(1S \rightarrow 1D)}$ , and  $k_{(1S \rightarrow 3S)}/k_{(1S \rightarrow 1F)}$ . The other forward rates  $k_{(1S \rightarrow 1F)}$  and  $k_{(1S \rightarrow 3S)}$  are then determined from the values of  $k_{(1S \rightarrow 1D)}$ , the ratios  $k_{(1S \rightarrow 1F)}/k_{(1S \rightarrow 1D)}$  and  $k_{(1S \rightarrow 3S)}/k_{(1S \rightarrow 1F)}$ , and the known degeneracies and energetics. Thus the determination of individual forward rate constants requires three measured quantities: the radiative lifetimes of the states involved, the total energy-transfer rate, and the ratio of rates into the product states.

#### IV. RESULTS

##### A. Radiative lifetimes and total energy-transfer rates

The radiative lifetimes and total relaxation rates are determined from the observed lifetimes of a given state at various buffer-gas pressures. The measured radiative lifetimes are shown in Table I for the  $1S_0$ ,  $1D_2$ , and  $1F_3$  states, along with a previous theoretical determination of the  $3S_1$  lifetime and earlier measured values of the  $1S_0$  and  $1D_2$  lifetimes.<sup>17,18</sup> The radiative lifetime of  $1S_0$  is measured directly at zero buffer-gas densities and also from the intercept of a plot of  $1/\tau_{\text{obs}}$  versus  $[M]$  by monitoring the 586.7-nm line. As shown in Table I both methods

TABLE I. Lifetimes of relevant excited states in atomic calcium.

State	$E$ (cm <sup>-1</sup> )	Lifetime (ns)		
$4s6s\ 1S_0$	40 690	92(±4) <sup>a</sup>	84(±10) <sup>b</sup>	89 <sup>c</sup>
$4p4p\ 1D_2$	40 719	19(±4) <sup>a</sup>	15.4 <sup>c</sup>	
$3d4p\ 1F_3$	40 537	41(±8) <sup>d</sup>		
$4s6s\ 3S_1$	40 474	33 <sup>e</sup>		

<sup>a</sup>Measured directly in this experiment at zero buffer-gas pressures.

<sup>b</sup>Measured from the intercept of  $1/\tau_{\text{obs}}$  vs pressure plots (see text).

<sup>c</sup>From the measurements of Havey *et al.* (Ref. 18).

<sup>d</sup>Measured from double exponential decay of  $1S \rightarrow 1F$  transfer experiment at near zero pressures.

<sup>e</sup>Taken from the theoretical calculations of Anderson *et al.* (Ref. 17).

agree very well. A previous measurement of the  $1S_0$  lifetime is also in excellent agreement with our results.<sup>18</sup> The  $1D_2$  lifetimes are only measured by exciting the  $1D_2$  state directly at zero buffer-gas densities and by observing the single exponential decay on the 585.7-nm line. This lifetime is also in excellent agreement with an earlier measurement.<sup>18</sup> The  $1F_3$  radiative lifetime is measured by pumping the  $1S_0$  state at very low buffer-gas pressure and monitoring the  $1F_3$  emission at 534.9 nm. At sufficiently low buffer-gas densities ( $< 2 \times 10^{15}$  atoms/cm<sup>3</sup>) this produces a double exponential fluorescence curve with one time constant being the  $1S_0$  lifetime and the other being the  $1F_3$  lifetime. The double exponential decay curves for the  $1F_3$  state are analyzed with a nonlinear least-squares routine and yield time constants of 41 ns for the rise and 100 ns for the decay. The 100-ns decay is attributed to the  $1S_0$ -state lifetime and the 41-ns rise is attributed to the  $1F_3$ -state lifetime. The collisional rates are much smaller than the radiative rates at these pressures and have only a small effect on the time dependence. The buffer-gas density is varied slightly to ensure that the collisional relaxation rates do not influence the measured radiative lifetime. The  $3S_1$  lifetime is taken from the calculations of Anderson *et al.*<sup>17</sup> These calculations predict a good value for the lifetime of another state of calcium,  $4s5p\ 3S_1$ , but they do not do so well for other states. For instance, the calculated lifetime for the  $1S_0$  is around 10 ns, which disagrees significantly with our measured value of 88 ns. This disagreement is probably due to the fact that the large amount of configuration interaction with the  $4p4p\ 1S_0$  state was not taken into account in the calculation. The calculations are probably reasonably good for  $3S_1$  since this state has a very small amount of configuration interaction or spin mixing.

An exponential decay time for the  $1S_0$  state is measured at each buffer-gas density. A plot of  $1/\tau_{\text{obs}}$  versus  $[M]$  has  $\Gamma_{(1S)}$  as intercept and  $k_q$  as slope. Figure 2 is a plot of  $1/\tau_{\text{obs}}$  versus  $[M]$  for the  $1S_0$  state upon collisions with all the rare gases at an oven temperature of 773 K. The straight lines are linear least-squares fits to the data. The average intercept is  $\Gamma_{(1S)}$ , which is also shown in Table I along with  $\Gamma_{(1S)}$  measured at zero buffer-gas density. The

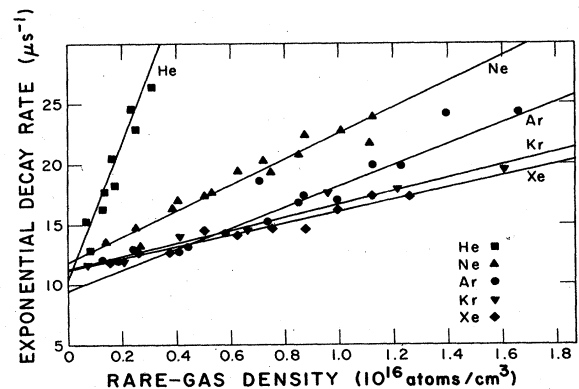


FIG. 2. Plot of the exponential decay rate ( $1/\tau_{\text{obs}}$ ) as a function of rare-gas density. Straight lines are linear least-squares fits to the data points.

TABLE II. Total Ca( $4s6s\ ^1S_0$ ) energy-transfer rate constant upon collisions with rare gases.

Rare gas	Rate ( $\text{cm}^3/\text{atom s}$ ) <sup>a</sup> ( $\pm 30\%$ ) <sup>b</sup>
<sup>3</sup> He	$6.4 \times 10^{-9}$
<sup>4</sup> He	$5.2 \times 10^{-9}$
Ne	$1.1 \times 10^{-9}$
Ar	$8.7 \times 10^{-10}$
Kr	$5.4 \times 10^{-10}$
Xe	$4.9 \times 10^{-10}$

<sup>a</sup>Measured in a static gas cell at 773 K.

<sup>b</sup>Error bars determined from weighted least-squares fit.

total energy-transfer rate constant  $k_q$  is derived from the slope and is tabulated in Table II for the rare gases. It should be noted that if the intercept for the  $1/\tau_{\text{obs}}$  versus  $[M]$  plots is constrained to go through the  $^1S_0$  lifetime that is measured at zero pressure, this results in only a 6% decrease in  $k_q$  for argon, which is the worst case. The error estimates listed in Table II consider both the standard deviation of the least-squares fit to the data and the random errors in the individual data points.

The sidearm temperature, which controls the calcium density in the oven, is a critical parameter in this experiment. At sidearm temperatures greater than 823 K (Ca density  $> 5 \times 10^{13}$  atoms/cm<sup>3</sup>), two severe interferences were discovered. The first is stimulated emission from the  $^1S_0$  state to the  $4s5p\ ^1P_1$  state at  $3.5\ \mu\text{m}$  following the dye-laser pulse. This causes the  $^1S_0$  lifetime to be shorter and the product-state intensity to be too small. The second interference is due to collisions between two excited states,<sup>19</sup> in this case most likely one calcium atom in the  $4s4p\ ^1P_1$  state and another in the  $4s3d\ ^1D_2$  state. This causes a long  $^1S_0$  emission and alters the product-state intensities. For both these reasons the sidearm temperature is maintained below 723 K (Ca density of  $2 \times 10^{12}$  atoms/cm<sup>3</sup>), where these interfering effects are not observed. No other effects such as radiation trapping were observed.

### B. Product-state collisional branching ratios and forward rate constants

At buffer-gas densities as low as  $\sim 1.2 \times 10^{14}$  atoms/cm<sup>3</sup>, emission is observed from the  $^1D_2$  and  $^1F_3$  product states following excitation of  $^1S_0$ . However, emission is not observed from the  $^3S_1$  state at any buffer-gas density used in this experiment (up to  $6.0 \times 10^{17}$  atoms/cm<sup>3</sup>). Also, following direct laser excitation of the  $^3S_1$  state, strong fluorescence is observed from the  $^3S_1$  state whereas no emission is observed from the other near-resonant states in the system. As discussed in Sec. III, by integrating a 15-ns portion of the product-state emission delayed 50 ns from the pump laser pulse, the detection factors are calibrated at high pressures where the populations are statistical, and then the ratios of rates (branching ratios) are determined at low pressures. This is done by monitoring the ratio of intensities of any two states. Signals are integrated by a boxcar averager and di-

vided by the total emission intensity from either the  $^1S_0$  or  $^1F_3$  state, discussed in Sec. III, in order to normalize for the laser excitation efficiencies. The intensity of each product state,  $^1D_2$  or  $^1F_3$ , is measured at each individual pressure by scanning the monochromator over the emission lines, after which the line area is integrated to give the total intensity. A sample spectrum of the  $^1D_2$ - and  $^1F_3$ -state emissions at 585.7 and 534.9 nm, respectively, is shown in Fig. 3 at a neon density of  $1.25 \times 10^{16}$  atoms/cm<sup>3</sup>.

The  $I_{(^1D_2)}/I_{(^1F_3)}$  intensity ratio is measured as a function of buffer-gas density for neon. The data are shown in Fig. 4. The data are fitted to the function

$$f(P) = a_1 + a_2 e^{-a_3 P}, \quad (14)$$

which approximates the pressure dependence expected at low pressure<sup>7</sup> and smoothly approaches equilibrium at high pressures. In the high-pressure limit the data fit the functional form  $a_1 + a_2/P$  better than Eq. (14); however, this function blows up as  $P \rightarrow 0$  and cannot be used. The values of the  $a_i$  for the fit in Fig. 4 are  $a_1 = 0.397$ ,  $a_2 = 0.729$ , and  $a_3 = 0.550$ . The value for  $a_1$  is directly related to the high-density limit  $(I_{(^1D_2)}/I_{(^1F_3)})_{\text{HP}}$  in Eq. (9) from which  $c_{(^1D_2)}/c_{(^1F_3)} = 0.74 (\pm 15\%)$  is obtained. The zero-pressure intercept  $a_1 + a_2$  is directly related to  $(I_{(^1D_2)}/I_{(^1F_3)})_{\text{LP}}$  of Eq. (8). Using these two ratios and the lifetimes from Table I in Eq. (8), the ratio of forward rates into  $^1D_2$  and  $^1F_3$  is determined. In Eq. (8) the exponential term in brackets for both the  $^1D_2$  and  $^1F_3$  states is equal to  $0.73 (\pm 20\%)$ . The ratio of rates for the other collision partners are determined by measuring the low-pressure intensity ratios only and then using Eq. (10) to get the ratio of rates relative to the data for neon. At average densities of  $1.2 \times 10^{14}$  cm<sup>-3</sup> (low-density limit in Fig. 4) we find the ratio of  $(I_{(^1D_2)}/I_{(^1F_3)})_{\text{LP}}$  to be 6.19, 5.13, 1.13, and 0.71 for <sup>3</sup>He, <sup>4</sup>He, Ne, and Xe, respectively (all are  $\pm 20\%$ , see Table III).

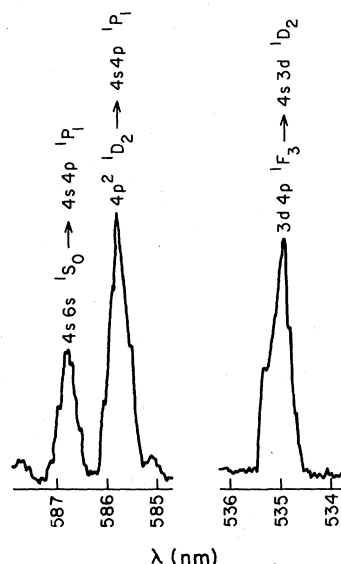


FIG. 3. Sample emission spectra of  $^1S_0$  initial state and  $^1D_2$  and  $^1F_3$  product states ( $[\text{Ne}] = 1.25 \times 10^{16}$  cm<sup>-3</sup>).

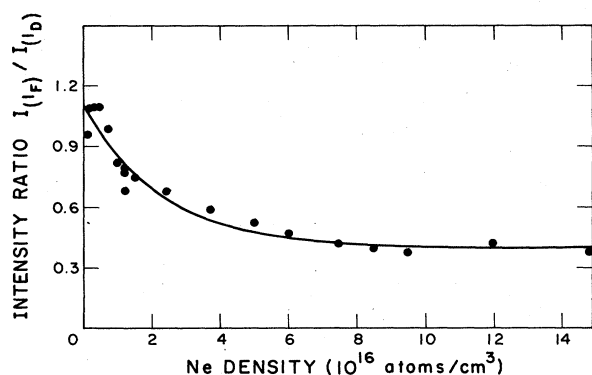


FIG. 4. Intensity ratio  $I_{(1D)}/I_{(1F)}$  as a function of neon density. Solid line is an iterative fit to Eq. (15) (see text).

The maximum  $^3S_1$  population, and thus the maximum rate into  $^3S_1$ , is estimated from the noise in the spectrum. The maximum intensity  $I_{(3S)}$  is less than the noise in the best spectra. With a neon buffer-gas density of  $1.3 \times 10^{17}$  atoms/cm<sup>3</sup>, one would predict from Eq. (11) that  $I_{(3S)}/I_{(1F)}$  would be 0.26 if the system were in equilibrium. However, the measured  $I_{(3F)}/I_{(1F)}$  is less than 0.001 and therefore the ratio of rates is less than 0.001/0.26 times a statistical ratio of rate constants. Since this limit is measured at high pressures it also includes the multiple collision processes  $^1S \rightarrow ^1D \rightarrow ^3S$  and  $^1S \rightarrow ^1F \rightarrow ^3S$ . A statistical ratio of rate constants is  $(g_{(3S)}/g_{(1F)}) \exp(-\Delta E/k_B T) = 0.38$ , so the ratio of rate constants is less than 0.0014. No  $^3S_1$  emission was observed when any of the other rare gases were used.

Table III shows the measured values for the ratio of rates with the rare gases used. These values are combined with the total energy-transfer rate constants in Table II to determine individual forward rate constants from Eq. (13). These individual forward rate constants are tabulated in Table IV. Also shown are thermally averaged cross sections, equal to the forward rates divided by the average relative velocity at 773 K. It should be noted that the increase in rate from  $^4\text{He}$  to  $^3\text{He}$  shows that there is a strong velocity dependence, and therefore the sensitivity of the cross sections quoted here will be very dependent on the specific velocities.

TABLE III. Ratios of forward rate constants to each product state.

Collision partner	$I_{(1S \rightarrow 1D)}$	$k_{(1S \rightarrow 1D)}$	$I_{(1S \rightarrow 3S)}$	$k_{(1S \rightarrow 3S)}$
	$I_{(1S \rightarrow 1F)}$ ( $\pm 20\%$ )	$k_{(1S \rightarrow 1F)}$ ( $\pm 32\%$ ) <sup>a</sup>	$I_{(1S \rightarrow 1F)}$	$k_{(1S \rightarrow 1F)}$
$^3\text{He}^b$	6.19	11.5		
$^4\text{He}^b$	5.13	9.5		
Ne <sup>c</sup>	1.13	2.1	< 0.001 <sup>d</sup>	< 0.0014 <sup>d</sup>
Xe <sup>b</sup>	0.71	1.3		

<sup>a</sup>This error bar is determined from a 15% uncertainty in detection factors, a 20% uncertainty in lifetimes, and a 20% uncertainty in the intensity ratio.

<sup>b</sup>Measured relative to the value for Ne.

<sup>c</sup>Measured directly using data in Fig. 4.

<sup>d</sup>Estimated from noise in the best spectra (see text). No  $^3S_1$  emission was observed from any of the other rare gases either.

## V. DISCUSSION

The individual forward rate constants in Table IV show very different trends in the rates to populate the different product states with buffer gas. Production of  $^3S_1$  is essentially forbidden for all the rare-gas collision partners. Transfer to the  $^1D_2$  state is a strong function of rare gas, going up sharply with increasing relative velocity, while  $^1F_3$  production is relatively independent of the buffer-gas collision partner. A detailed discussion of these results requires a knowledge of all of the potential-energy curves and matrix elements. However, the small size of the  $^3S_1$  rate constant allows certain qualitative statements to be made concerning the spin-changing process. Also, the large rate into the  $^1D_2$  level and its near resonance with the  $^1S_0$  state allows simple theories to be applied where long-range dispersion forces can be used as a first approximation to the actual potentials. Transfer to the  $^1F_3$  state is more typical of a curve-crossing event. It is more difficult to say very much about the dynamics involved without more detailed information about the potential curves.

The small rate constant for transfer from any of the singlet states to the  $^3S$  state can be due to two related effects. Either the quasimolecular potential curves cross but have a vanishingly small matrix element, or they do not cross (interact) at the accessible energies. The latter possibility can almost certainly be ruled out since the attractive parts of the  $^1D_2$  and  $^1F_3$  potentials will cross both the  $^1S$  and the  $^3S$  potentials, allowing the states to couple. Thus we can consider the process to be governed by the strength of the singlet-to-triplet mixing. In light of this, the small probability for spin changing is best explained by a very small spin-orbit matrix element coupling the molecular singlet and triplet states at the curve crossing. Thus, the singlet  $\rightarrow ^3S$  process may accurately be described as a pure spin-changing process because of the small amount of spin mixing in the isolated atomic states. In an earlier study of the  $^1P \rightarrow ^3P$  curve crossing,<sup>7</sup> it is very likely that the efficiency of the spin change there is due to an interaction between the parts of the wave function with similar spin in the isolated atom states.

For the  $^1S_0 \rightarrow ^1D_2$  process, only a very long-range interaction can give rise to such very large cross sections. For an atom the size of the  $4s6s\ ^1S_0$  state of calcium, one

TABLE IV. Individual forward rate constants and thermally averaged cross sections ( $T=773$  K). [All errors are  $\sim \pm 40\%$ . The error bars are determined from the error bars on both the total energy-transfer rate ( $\pm 30\%$ ) and the ratio of rates ( $\pm 30\%$ ).]

Collision partner	$k_{(1S \rightarrow 1D)}$ cm <sup>3</sup> /atom s	$\sigma_{(1S \rightarrow 1D)}$ (Å <sup>2</sup> )	$k_{(1S \rightarrow 1F)}$ cm <sup>3</sup> /atom s	$\sigma_{(1S \rightarrow 1F)}$ (Å <sup>2</sup> )	$k_{(1S \rightarrow 3S)}$ cm <sup>3</sup> /atom s	$\sigma_{(1S \rightarrow 3S)}$ (Å <sup>2</sup> )
<sup>3</sup> He	$4.8 \times 10^{-9}$	213	$4.3 \times 10^{-10}$	19		
<sup>4</sup> He	$3.9 \times 10^{-9}$	199	$4.2 \times 10^{-10}$	21		
Ne	$6.1 \times 10^{-10}$	59	$6.1 \times 10^{-10}$	29	$3.1 \times 10^{-13}$	<0.03
Xe	$2.4 \times 10^{-10}$	35	$1.8 \times 10^{-10}$	26		

does not expect a curve crossing at such a large radius, especially for the helium collision partner. Also, the fact that at large distances the Ca–rare-gas potential curves vary only slightly from the isolated atom energies leads us to conclude that this process need not be due to a localized curve crossing, but rather can be due to an interaction which leads to state changes at long range between relatively parallel potentials. Since the collision partner is always a rare gas which is spherically symmetric and is left unchanged after the collision, one must use the second-order induced-dipole potential to couple the  $1S$  to the  $1D$  state.<sup>15</sup> The  $1S_0$  state can actually be written as  $|1S_0\rangle = 0.80|4s6s1S_0\rangle + 0.40|4p4p1S_0\rangle$ , where the amount of wave-function mixing is estimated from quantum-defect measurements.<sup>9,10</sup> In second-order perturbation theory one can change the electron orbital angular momentum by 0,  $\pm 2$  with dipole forces. Thus both the  $4s6s$  and  $4p4p$  parts of the initial  $1S_0$  can couple to the  $4p4p1D_2$  product with dipole forces.<sup>15</sup>

Several theoretical studies have been performed on the long-range, noncrossing transfer mechanism described above. Stuckelberg first considered the problem from a wave treatment point of view.<sup>20</sup> More recently Bates,<sup>12</sup> Vainshtein *et al.*,<sup>13</sup> Presnyakov,<sup>14</sup> and Gurnee and Magee<sup>21</sup> have used impact-parameter methods to solve this two-state problem. Making improvements over the earlier work, Nakamura<sup>22</sup> and Nikitin<sup>3</sup> discuss aspects of the various treatments with the conclusion that it is difficult to determine which approximate solution should be used in a particular case. It is therefore useful to compare several of these solutions to our experimental results. However, since the exact wave functions and polarizabilities of the excited calcium states are not known, only the relative sizes of the rates as a function of rare gas will be compared to the experimental results.

The general method for determining the approximate solutions is briefly described below. The total Hamiltonian for the two-atom interaction is written

$$H = H_0 + H', \quad (15)$$

where  $H_0$  is the Hamiltonian for the isolated atoms and  $H'$  is the time-dependent interaction Hamiltonian. In the two-state approximation, neglecting minor variations in the energy with interatomic separation, the wave function is written as

$$\psi(t) = c_1(t)\phi_1 e^{-iE_1 t/\hbar} + c_2(t)\phi_2 e^{-iE_2 t/\hbar}, \quad (16)$$

where  $\phi_1$  and  $\phi_2$ , and  $E_1$  and  $E_2$  are the eigenfunctions and eigenvalues of the separated-atom Hamiltonian  $H_0$ , and  $c_1$  and  $c_2$  are the expansion coefficients.  $\phi_1$  and  $\phi_2$  are simply given by the product of the separated-atom wave functions [i.e.,  $\phi_1 = \psi(\text{Ca } 4p4p1S_0)\psi(\text{RG ground } 1S_0)$ , etc.]. Diagonal matrix elements are neglected here since at large distances they are small compared to the energy separation of the initial and final states,  $\Delta E$ . Insertion of Eq. (16) into the time-dependent Schrödinger equation yields the set of coupled differential equations

$$i\hbar\dot{c}_1(t) = c_2(t)H_{12}e^{i\omega t}, \quad (17a)$$

$$i\hbar\dot{c}_2(t) = c_1(t)H_{21}e^{-i\omega t}, \quad (17b)$$

where  $\omega = \Delta E/\hbar$  and  $H_{12} = H_{21} = \langle \phi_2 | H' | \phi_1 \rangle$ . The initial conditions are taken to be  $c_1(-\infty) = 1$  and  $c_2(-\infty) = 0$ . The desired solution is the probability of being in state 2 after the collision,  $P_{12} = |c_2(\infty)|^2$ . It is the approximate solution of Eq. (17) to obtain  $P_{12}$  that is the subject of the several theoretical works mentioned above.

A two-center expansion of the calcium–electron–rare-gas–electron interaction term,<sup>23</sup>  $1/|r_i - r_j|$ , in the Hamiltonian  $H'$ , reveals the multiple interaction terms between the atoms. The largest nonvanishing term for this multipole interaction in second-order perturbation theory will be due to induced-dipole interactions. This matrix element is derived from second-order perturbation theory and after simplification can be written<sup>15</sup> for a one-electron system as

$$H_{12} = -\frac{1}{2} \frac{\alpha_{\text{RG}} e^2}{R_{ab}^6} \langle \psi_{(1S)} | r^2(\cos^2\theta + 1) | \psi_{(1D)} \rangle, \quad (18)$$

where  $\psi_{(1S)}$  and  $\psi_{(1D)}$  are the atomic wave functions,  $\alpha_{\text{RG}}$  is the rare-gas polarizability,<sup>24</sup> and  $R_{ab}$  is the internuclear distance. Since the radial parts of the calcium wave functions are not known we will simply approximate them as hydrogenic orbitals.<sup>25</sup> With known screening constants<sup>26</sup> and approximating the  $4p4p1D_2$  wave function as the hydrogenic orbital  $4s5d1D_2$  one obtains  $\langle \psi_{(1S)} | r^2(\cos^2\theta + 1) | \psi_{(1D)} \rangle \cong 146a_0^2$ . The polarizabilities of the rare gases are taken from the literature.<sup>24</sup>

Rosen and Zener<sup>27</sup> postulated a general solution to Eq. (17) and Bates<sup>12</sup> obtained general solutions for  $A/R^n$  matrix elements. For  $n = 6$  one obtains

$$P_{(1S \rightarrow 1D)}(b, \nu) = \frac{1}{9}(\gamma^2 b^2 + 3\gamma b^2 + 3)^2 \times \exp(-2\gamma b) \sin^2(3\pi\beta/8b^5), \quad (19)$$

where  $\gamma = \Delta E / \hbar v$  and  $\beta = A / \hbar v$ ,  $b$  is the impact parameter, and  $v$  is the relative velocity. Skinner<sup>28</sup> has shown for some special cases that this approximate solution matches the exact numerical solution of Eq. (17) in the region  $\gamma < 1$  (in atomic units). For the worst case in this experiment, Ca-Xe, one finds  $\gamma = 0.42$  for the average thermal velocity. Using a different technique, Vainshtein *et al.*<sup>13,14</sup> considered the case where  $\Delta E$  is not constant, with the result that for  $n = 6$ .

$$P_{(1S \rightarrow 1D)}(b, v) = \sin^2 \left[ \frac{3\pi\beta}{8b^5} \right] \times \exp \left\{ - \left[ 2^{7/3} \beta^{1/3} \gamma^{5/3} \sin^2 \left[ \frac{\pi}{12} \right] + 4\gamma^2 b^2 \right]^{1/2} \right\}, \quad (20)$$

where here the variation in  $\Delta E$  is due to  $H_{12}$  only.

In the semiclassical approximation the internuclear distance  $R$  is written  $R = (b^2 + v^2 t^2)^{1/2}$  where  $b$  is the impact parameter. However, the function  $A/R^6$  blows up for small impact parameters and time, thus producing an unrealistically large matrix element. To alleviate this problem the transition probability is truncated at small impact parameters and set equal to  $g_{(1D)}/(g_{(1D)} + g_{(1S)})$  when  $P(b, v)$  becomes large. Equation (18) is only meant to be a first guess at the absolute value of the matrix element and it allows an approximate determination of the trend of the matrix element with rare gas.

Cross sections from both Eqs. (19) and (20) are calculated from

$$\sigma(v) = 2\pi \int_0^\infty b P(b, v) db, \quad (21)$$

which is numerically integrated to obtain  $\sigma$  as a function of velocity. The cross-section calculations of Nakamura<sup>22</sup> for a first-order dipole interaction between excited and ground-state hydrogen shows a similarity among the general methods of Bates,<sup>12</sup> Vainshtein *et al.*,<sup>13</sup> and Presnyakov;<sup>14</sup> however, there is a rather large difference in the absolute values with Bates's treatment typically

producing a larger calculated cross section. The forward rate constant is then determined at temperature  $T$  from

$$k(T) = \int_0^\infty v \sigma(v) f(v, T) dv, \quad (22)$$

where  $f(v, T)$  is a Maxwell-Boltzmann velocity distribution at temperature  $T$ .

Both Eqs. (19) and (20) behave similarly as a function of impact parameter, velocity, and matrix element. For both equations,  $bP_{(1S \rightarrow 1D)}$  is maximum at an impact parameter of approximately  $20a_0$  for the matrix elements of this system. However, the decrease in  $bP_{(1S \rightarrow 1D)}$  with increased impact parameter is slowly varying and most of the transition probability is determined at impact parameters greater than  $15a_0$ . The numerically evaluated cross sections increase with increasing velocity (approximately linear) and the rate constant increases with increased temperature (also linear). These increases are consistent with the fact that Eqs. (19) and (20) are both basically proportional to the square of the Fourier frequency component of  $H_{12}$  at  $\omega = \Delta E / \hbar$ , and this component increases with velocity in our range of matrix elements and velocities.

The numerically calculated rate constants are shown in Table V. As mentioned earlier, for these simplified calculations the relative magnitudes of the rates compared to  $k_{(1S \rightarrow 1D)}(^3\text{He})$  are of more importance than the actual rates, since the exact atomic wave functions and thus the matrix elements are not well known. It can be seen in Table V that both of the theories predict the relative trend in the rates reasonably well. The formalism of Bates<sup>12</sup> has a stronger dependence on matrix element than the formalism of Vainshtein *et al.*<sup>13</sup> and Presnyakov.<sup>14</sup> Although the relative rates are changed significantly when the matrix element is changed by an order of magnitude, the same basic trend with rare gases is preserved. The general agreement between experiment and theory supports the long-range induced-dipole transition mechanism.

It should be mentioned that the neglect of the adiabatic energy changes may be a significant source of error in these calculations. Dipole forces decrease rapidly and  $bP(b, v)$  peaks with  $b$  at separations where the diagonal matrix elements may be the same order of magnitude as  $\Delta E$ . Since all of the simple theories show a strong depen-

TABLE V. Comparison between experimental and theoretical values for relative rates into  $1D_2$ .

Collision partner	Relative rate $k_{(1S \rightarrow 1D)}(\text{RG})/k_{(1S \rightarrow 1D)}(^3\text{He})$ and, in parentheses, $k_{(1S \rightarrow 1D)}(\text{cm}^3/\text{atom s})$		
	Experimental ( $\pm 40\%$ ) <sup>a</sup>	Bates method ( $\pm 81.0\%$ ) <sup>b</sup>	Vainshtein method ( $\pm 21\%$ ) <sup>b</sup>
<sup>3</sup> He	1.0 ( $4.8 \times 10^{-9}$ )	1.0 ( $1.4 \times 10^{-9}$ )	1.0 ( $3.0 \times 10^{-10}$ )
<sup>4</sup> He	0.81 ( $3.9 \times 10^{-9}$ )	0.86 ( $1.2 \times 10^{-10}$ )	0.73 ( $2.2 \times 10^{-10}$ )
Ne	0.12 ( $6.1 \times 10^{-10}$ )	0.37 ( $5.2 \times 10^{-10}$ )	0.14 ( $4.3 \times 10^{-11}$ )
Xe	0.049 ( $2.4 \times 10^{-10}$ )	0.15 ( $2.1 \times 10^{-10}$ )	0.03 ( $7.9 \times 10^{-12}$ )

<sup>a</sup>Experimental error bars.

<sup>b</sup>These error bars are determined by varying the matrix element by an order of magnitude. It is not an estimate of the methods' accuracy.

dence on energy gap, it is expected that this will cause a large change in the rate constants. Since the inclusion of diagonal matrix elements would affect all of the rates for the different rare gases in a similar manner, it is felt that this may cause a significant change in the relative rates.

We attempted to predict the  $^1S \rightarrow ^1F$  rates by using the long-range mechanism above with the appropriate changes in matrix element. The results of performing such a calculation give an incorrect trend with rare gas as well as several orders of magnitude smaller values than the experimentally observed relative rates. Although the long-range interactions are present, they are weaker compared to the size of the energy separation. This is due to the fact that the  $^1S \rightarrow ^1F$  process requires more complicated forces than dipole forces, which only take on large values at slightly smaller distances, and the fact that the energy separation is larger, resulting in a larger frequency component needed for the transition. Indeed, the  $^1S \rightarrow ^1F$  rate is more likely to be governed by a localized curve-crossing interaction. As discussed in our previous work,<sup>7</sup> it is not possible to discuss such a mechanism without proper potential-energy curves and matrix elements. This problem is further complicated by the fact that the

$^1S \rightarrow ^1D$  process can occur early in the collision and then it is uncertain whether a  $^1S \rightarrow ^1F$  or an indirect  $^1S \rightarrow ^1D \rightarrow ^1F$  transition populates the  $^1F$  state. Thus there is some question whether the two-state model is completely applicable here.

In conclusion, the spin-changing process  $^1S \rightarrow ^3S$  is found to be immeasurably small in this system. There is very little spin mixing present and this small rate is attributed to a very small spin-orbit matrix element. The very large  $^1S \rightarrow ^1D$  rates are explained rather well by long-range dipole-induced forces acting through second-order induced-dipole potentials. This mechanism works since the  $^1S$  and  $^1D$  atomic states are so close in energy; their closeness is a direct result of configuration interaction in calcium. The  $^1S \rightarrow ^1F$  rates are thought to be due to a more localized curve-crossing process, for which detailed potentials would be required to explain further their trend with rare gas.

#### ACKNOWLEDGMENT

The authors gratefully acknowledge the support of the National Science Foundation.

\*Quantum Physics Division, National Bureau of Standards.

<sup>1</sup>L. Krause, *Adv. Chem. Phys.* **28**, 267 (1975).

<sup>2</sup>P. L. Lijnse, Fysich Laboratorium Utrecht University Report No. i398, 1972 (unpublished).

<sup>3</sup>E. E. Nikitin, *Adv. Chem. Phys.* **28**, 317 (1975).

<sup>4</sup>W. H. Breckenridge and H. Umemoto, *Adv. Chem. Phys.* **50**, 325 (1982).

<sup>5</sup>H. J. Yuh and P. J. Dagdigan, *Phys. Rev. A* **28**, 63 (1983).

<sup>6</sup>M. H. Alexander, T. Ovlkowski, and J. E. Straub, *Phys. Rev. A* **28**, 73 (1983).

<sup>7</sup>M. O. Hale and S. R. Leone, *J. Chem. Phys.* **79**, 3352 (1983).

<sup>8</sup>E. U. Condon and G. H. Shortley, *The Theory of Atomic Spectra* (Cambridge University, Cambridge, England, 1979).

<sup>9</sup>K. T. Lu, *J. Opt. Soc. Am.* **65**, 706 (1974).

<sup>10</sup>J. A. Armstrong, P. Esherich, and J. J. Wynne, *Phys. Rev. A* **15**, 180 (1977).

<sup>11</sup>G. Risberg, *Ark. Fys.* **37**, 231 (1967).

<sup>12</sup>D. R. Bates, *Discuss. Faraday Soc.* **33**, 7 (1962).

<sup>13</sup>L. Vainshtein, L. Presnyakov, and I. Sobelman, *Zh. Eksp. Teor. Fiz.* **43**, 518 (1963) [*Sov. Phys.—JETP* **16**, 370 (1963)].

<sup>14</sup>L. P. Presnyakov, *Proc. P. N. Lebedev, Phys. Inst. [Acad. Sci.*

(USSR)] **30**, 191 (1964).

<sup>15</sup>J. Callaway and E. Bauer, *Phys. Rev.* **140A**, 1072 (1965).

<sup>16</sup>R. E. Honig, *RCA Rev.* **18**, 195 (1957).

<sup>17</sup>E. M. Anderson, V. A. Zilitis, and S. E. Sorokina, *Opt. Spektrosk.* **23**, 513 (1967) [*Opt. Spectrosc. (USSR)* **23**, 279 (1967)].

<sup>18</sup>M. D. Havey, L. C. Balling, and J. J. Wright, *J. Opt. Soc. Am.* **67**, 488 (1977).

<sup>19</sup>J. Huennekens and A. Gallagher, *Phys. Rev. A* **27**, 771 (1983).

<sup>20</sup>E. C. G. Stuckelberg, *Helv. Phys. Acta* **5**, 369 (1932).

<sup>21</sup>E. F. Gurnee and J. L. Magee, *J. Chem. Phys.* **26**, 1237 (1957).

<sup>22</sup>H. Nakamura, *J. Phys. Soc. Jpn.* **20**, 2272 (1965).

<sup>23</sup>J. O. Hirschfelder, C. F. Curtis, and R. B. Bird, *Molecular Theory of Gases and Liquids* (Wiley, New York, 1954).

<sup>24</sup>J. F. Hornig and J. O. Hirschfelder, *J. Chem. Phys.* **20**, 1812 (1982).

<sup>25</sup>H. A. Bethe and E. E. Salpeter, *Quantum Mechanics of One- and Two-Electron Atoms* (Plenum, New York, 1977).

<sup>26</sup>E. Clementi and D. L. Raimondi, *J. Chem. Phys.* **38**, 2686 (1963).

<sup>27</sup>N. Rosen and C. Zener, *Phys. Rev.* **40**, 562 (1932).

<sup>28</sup>B. G. Skinner, *Phys. Rev.* **40**, 502 (1932).